Revista Brasileira de Meteorologia, **v. 39,** e39240004, 2024
DOI: http://dx.doi.org/10.1590/0102-77863910004

Article

Radiation Balance over Low-Turbidity Water Artificially Cleaned for Irrigation of Tobacco Grown Under Shading. I. Analysis of the Shortwave and Longwave Components

Tatyana Keyty de Souza Borges[1], Aureo Silva de Oliveira[2], Richard G. Allen[3], Ayse Kilic[4], João Paulo Chaves Couto[2], Carlos Eduardo Santana[5]

[1]*Instituto Federal de Educação, Ciência e Tecnologia do Sertão Pernambucano, Ouricuri, PE, Brazil.*
[2]*Centro de Ciências Agrárias, Ambientais e Biológicas, Universidade Federal do Recôncavo da Bahia, Cruz das Almas, BA, Brazil.*
[3]*University of Idaho, Kimberly, USA*
[4]*University of Nebraska, Lincoln, USA*
[5]*DANCO Comércio e Indústria de Fumos Ltda, Governador Mangabeira, BA, Brazil.*

Received: 18 January 2023 - Accepted: 13 June 2024

Abstract

In eastern sub-humid Bahia, Brazil, surface water stored in lined ponds is used to drip irrigate Sumatra tobacco plants grown under partial shading. This work, as part of a large evaporation study, aimed at monitoring, over two irrigation seasons (2015 and 2016), the water turbidity, the radiation balance (shortwave - SW and longwave - LW components), and the skin water temperature (T_w) with sensors deployed in a raft. The water turbidity was very low (around 2.6 NTU on average) due to filtration and reverse osmosis treatment of water prior to storage. Considering data from both seasons, the net SW radiation S_{net} was about 96% of incoming SW flux S_g. The daily net LW flux L_{net} was consistently negative (-55.1 W/m^2 average). The net all-wave radiation R_n corresponded to 77% of S_{net}. Four days were selected from both seasons to evaluate the effects of cloudiness on the SW and LW components. While S_{net} decreased with cloudiness due to solar radiation blockage, L_{net} also decreased but due to increasing of downward LW radiation L_{atm} with cloudiness. R_n also decreased with cloud cover. Based on the 2015 data, on average, daily T_w (26.1 °C) was higher than air temperature T_a (21.8 °C) due to near-surface absorption of solar radiation with T_a showing a much higher daily amplitude.

Keywords: solar radiation, atmospheric radiation, water turbidity, tobacco.

Balanço de Radiação sobre Água de Baixa Turbidez Purificada Artificialmente para Irrigação de Fumo Cultivado sob Sombreamento. I. Análise dos Components de Onda Curta e Onda Longa

Resumo

No leste subúmido da Bahia, Brasil, água de superfície armazenada em reservatórios revestidos é usada para irrigar por gotejamento plantas de fumo tipo Sumatra cultivadas sob sombreamento parcial. Este trabalho, no âmbito de um estudo maior sobre evaporação, teve como objetivo monitorar, durante duas estações de cultivo (2015 e 2016), a turbidez da água, o balanço de radiação (componentes de onda curta - OC e onda longa - OL) e a temperatura superficial da água (T_w), com sensores instalados numa plataforma flutuante. A turbidez da água era muito baixa (cerca de 2,6 NTU em média) devido à filtragem e tratamento osmose reversa antes do armazenamento. Com base nos dados de ambas as esta-

Corresponding author: Tatyana Keyty de Souza Borges. E-mail: tatyana.borges@ifsertao-pe.edu.br.

ções, a radiação líquida de OC S_{net} correspondeu a cerca de 96% da radiação de OC incidente S_g. O saldo diário de OL L_{net} foi consistentemente negativo (média de -55,1 W/m^2). A radiação líquida total R_n correspondeu a 77% de S_{net}. Quatro dias foram selecionados (dois de cada ano) para avaliar os efeitos da nebulosidade nos componentes de OC e OL. Enquanto S_{net} diminuiu com a nebulosidade devido ao bloqueio da radiação solar, L_{net} também diminuiu, mas devido ao aumento da radiação OL incidente L_{atm} com a nebulosidade. R_n também diminuiu com a cobertura de nuvens. Com base nos dados de 2015, em média, a T_w diária (26,1 °C) foi maior que a temperatura do ar T_a (21,8 °C) devido à absorção da radiação solar pela superfície, T_a mostrando uma amplitude diária muito maior.

Palavras-chave: radiação solar, radiação terrestre, turbidez da água, fumo.

1. Introduction

The surface radiation balance describes the energy converted into sensible and latent heat or into heat storage for a large spectrum of processes at the lower boundary of the atmosphere. Its knowledge is of paramount importance in many fields of study including hydrology, biology, agriculture, and meteorology. In lakes and reservoirs, for example, the amount of water evaporated is a function of the radiation balance at the surface.

Two radiative properties of a surface (albedo and emissivity) dictate the partitioning of shortwave (SW) and longwave (LW) radiation, respectively. Albedo (α) characterizes the fraction of incoming SW radiation that is reflected back by the surface while emissivity (ε) describes the amount of LW radiation that a surface emits relative to a black body at the same temperature (Monteith and Unsworth, 2013).

After reaching a water surface, incoming SW radiation penetrates to a depth that depends on water turbidity (transparency) - an optical property that is a function of suspended sediment concentration and dissolved colored materials (Marquis, 2005). Generally, the infra-red portion of radiation is strongly absorbed in the very thin surface layer while the bluish-green light, within the visible portion, penetrates the farthest in optically clear water (Davies-Colley and Smith, 2001; Jensen and Allen, 2016).

The downward flux of LW radiation is a function of air temperature and water vapor content in the air. Besides these two, the degree of cloud cover is also considered in the modelling of atmospheric emissivity (Carmona *et al.*, 2014; Silva *et al.*, 2019; Aimi *et al.*, 2021). Natural surfaces (soil, vegetation, and water) resemble a black body in the spectral range of terrestrial radiation (3-100 μm) with ε near 1 according to the Kirchhoff's law, which states that at the same temperature and wavelength good thermal absorbers are good thermal emitters. For water and other natural surfaces, it is common the use of the difference (1 - ε) as an approximation for the fraction of the atmospheric LW radiation that is reflected by the surface (Oke, 1995; Moene and Van Dam, 2014). This reflectance is a small fraction, varying from 1% to 5%, a reason why many studies assume ε = 1, including water (Finch and Hall 2005). Davies *et al.* (1971) found water emissivity for Lake Ontario to be constant at 0.972 while Shuttleworth (2012) suggested values ranging from 0.92 to 0.97 at small and large zenith angles.

A four-component net radiometer can measure all the SW and LW components of the radiation balance over a surface from which the net all-wave radiation (R_n) can be derived. Comparisons among instrument types have been extensive (Kohsiek *et al.*, 2007; Blonquist *et al.*, 2009). Measurement or estimation of R_n has been conducted over a variety of land-covers including lakes and reservoirs (Gianniou and Antonopoulos, 2007; Liu *et al.*, 2015; Aydin and Karakus, 2016).

Farm ponds have great potential to improve agricultural water security and crop production in many parts of the world (Gallego-Elvira et al., 2010). A good example is the cultivation of tobacco in eastern Bahia, Brazil, where this crop is drip-irrigated with low-turbidity surface water derived from reverse osmosis and stored in plastic-lined ponds. Due to the peculiarities of this type of water and considering the tropical characteristics of the region that favor water loss by evaporation, the objective of this work was to study the magnitude and time distribution of SW and LW components of the radiation balance as well as surface temperature of stored water from measurements carried out in the center of a pond. The influence of cloudiness on all components was also considered. This study on radiation balance is part of a larger study (Borges, 2017) on overall surface energy balance for the storage ponds including evaporation.

2. Material and Methods

2.1. Description of the experimental site

The site was in a private farm owned by a company whose business is to grow, process and export a special type of tobacco (*Nicotiana tobacco L.*) known as Sumatra. The leaves of this variety are exclusively used for wrapping cigars. The farm is located in the municipality of Governador Mangabeira, Bahia, Brazil (12°37' S, 39°03' W, 218 m asl) where the climate is a transition between Af (tropical without dry season) and Am (tropical monsoon) climates according to the Köppen system (Alvares *et al.*, 2013). The mean annual precipitation, air temperature, and relative humidity are around 1100 mm, 25 °C and 75%, respectively. The wind blows mainly from the southeast direction along the year at a 2.5 m/s average speed.

The crop grows under a black nylon mesh for partial shading and is drip irrigated. The cigar cover burns more

uniformly when chlorine-free water is used for irrigation and, therefore, after being filtered to eliminate solid particles (organic and inorganic) the pumped surface water is passed through a reverse osmosis system to remove salts, after which it is stored in lined reservoirs with a high degree of transparency (low turbidity). The artificial reservoirs are lined with 2-mm thickness sheets of welded HDPE black plastic. The reservoirs in the farm have trapezoidal cross-sections, with maximum depth varying from 4 to 8 m and storage capacities ranging from 5,000 to 30,000 m^3. About twelve reservoirs supply water from September to March every season to irrigate, on average, 150 ha of Sumatra tobacco.

2.2. Instrumentation and data acquisition

Experimental data were collected above water during the second semesters of 2015 and 2016 using instruments mounted on-board a handmade raft (Fig. 1). Details on the design and operation of this platform can be found in Borges *et al.* (2016). In 2015, the raft was positioned in the center of the water mirror of a reservoir having dimensions of 35-m wide (east-west direction) and 85-m long (north-south direction), with 50° average inclination walls, and with an initial water depth of 5.5 m. Total vertical height from pond bottom to the top of the sides was 6.3 m. In 2016, the reservoir used was deeper with a total vertical height of 8.2 m and 7.5 m of initial water depth. In both cases, the raft was anchored to the sides of the reservoir by means of nylon ropes.

The radiation balance components at the water surface were measured with a four-component net radiometer (model CNR4, Kipp & Zonen). The CNR4 consists of four thermopile sensors with two in the upper face to detect radiation from above and the other two in the lower face to detect radiation from the surface. The pyranometers (SW sensors) work in the spectral range of 305 to 2,800 nm and the pyrgeometers (LW sensors) in the range of 4,500 to 42,000 nm. Sensors of the same type are back facing. The field of view of sensors is 150° in the lower face and 180° in the upper one. During the measurements, the internal temperature of the net radiometer was monitored for correction of detected LW radiation. More technical specifications on the CNR4 can be found in Kipp & Zonen (2010) and Campbell Scientific (2014), including the accuracy intervals. Water turbidity measurements (NTU) were taken with a turbidimeter (model OBS3+, Campbell Scientific), positioned at 2 m depth.

The CNR4 was positioned 1.15 m above the surface at the end of a 3-m length metal boom pointing north. This configuration helped to minimize interference by the raft material on the outgoing radiation detected by the sensors. At that height, 99% of the SW and LW radiative fluxes in the underside of the instrument came from a footprint area of 415 m^2, equivalent to a circle having 11.5 m radius, smaller than the minimum distance (17 m) from the instrument to the water edge. In the same boom, an infrared thermometer (model SI-111, Apogee Instruments) was deployed (Fig. 1A), oriented perpendicular to the surface, for which the footprint area was 0.60 m^2 eliminating, therefore, effects of the raft on the sensor signal.

The measured outputs of the CNR4 in W/m^2 are the incoming SW (S_g) and LW (L_{atm}) radiation, and the surface-reflected SW (S_r) and the outgoing LW (L_s) radiation. The datalogger output table also included the net SW radiation ($S_{net} = S_g - S_r$) and the net LW radiation ($L_{net} = L_{atm} - L_s$) at the surface as well as the surface albedo ($\alpha = S_r/S_g$) and the net all-wave radiation ($R_n = S_{net} - L_{net}$).

The L_s component consists of two parallel fluxes (Monteith and Unsworth, 2013): (i) the LW flux emitted

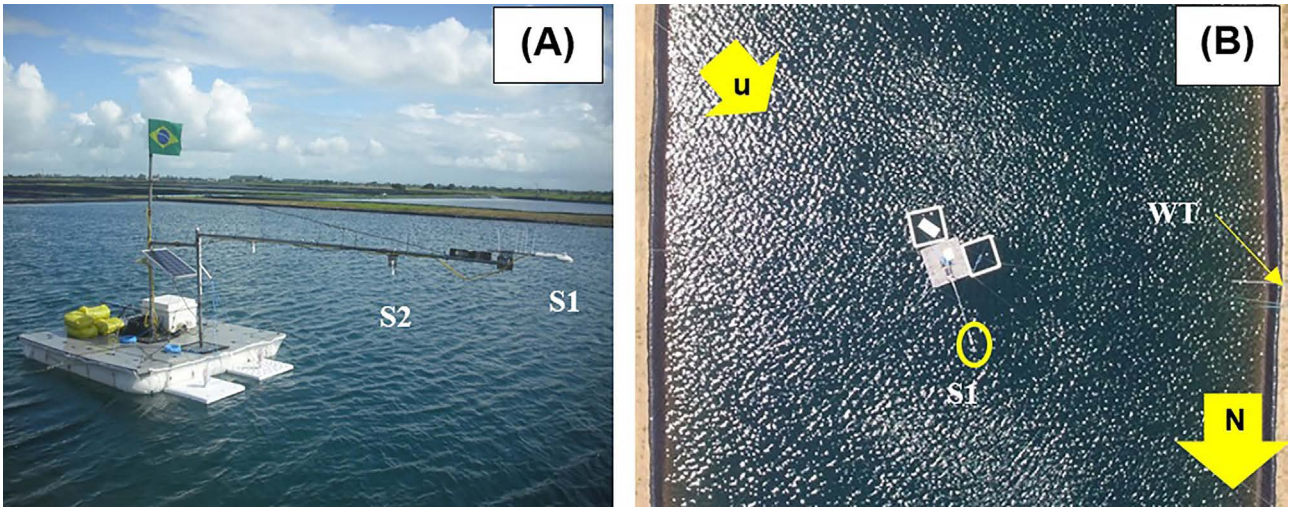

Figure 1 - The raft with a four-component net radiometer (S1) and an infrared thermometer (S2) in the 2015 (A) and 2016 (B) campaigns. (u = predominant wind direction, WT = weather tower position).

by water as a function of its emissivity (ε_w) and absolute temperature according to the Stefan-Boltzmann law and (ii) the incoming LW flux reflected by water. The relationship between them is given by Eq. (1).

$$L_e = L_s - L_r \quad (1)$$

where L_e is the surface-emitted and L_r is the surface-reflected LW radiation, both in W/m^2.

In the spectral range of atmospheric emission, the absorptivity of natural surfaces (ϕ) is equal to its emissivity (ε) (Monteith and Unsworth, 2013). For this study, we adopted $\phi_w = \varepsilon_w = 0.97$ (Davies *et al.*, 1971), which means that L_r of the low-turbidity water surface corresponded to 3% of L_{atm} according to Eq. (2).

$$L_r = (L_{atm} - \phi_w L_{atm}) = (1 - \varepsilon_w)L_{atm} = 0.03L_{atm} \quad (2)$$

Additional atmospheric data were obtained with a tripod-mounted weather tower (WT, Fig. 1B) located in the 2-m wide row between irrigation water tanks. The rows were covered with grass and are used for the transit of people in the everyday routine of maintenance. The WT was equipped with a thermo-hygrometer (model HMP60, Vaisala) at 2 m above the ground; an anemometric set for wind direction and speed (model 03001, RM Young) at 7 m height in 2015 and 3 m height in 2016; a thermopile pyranometer (model LP02, Hukseflux Thermal Systems) in 2015 and a silicon-cell pyranometer (model SPLite, Kipp & Zonen) in 2016, both positioned 2.5 m above ground surface. In both seasons, a rain gauge (model TE525MM, Texas Electronics) was used with the top cross-section at 0.5 m height. All sensors at the raft and WT were scanned every 30 seconds with a CR1000 datalogger (Campbell Scientific). Total and mean values were stored at subhourly (5 and 30 min), hourly and daily time steps for further analysis.

Atmospheric conditions influence the magnitude of the radiation balance components at the surface. Clouds partially block the passage of solar radiation and increase atmospheric LW emission (Moene and Van Dam, 2014). In this work, the atmospheric transmissivity for SW radiation calculated with data from the pyranometers at the WT was used to characterize mean daytime cloudiness on a daily basis, according to Eq. (3).

$$\tau_{atm} = \frac{S_g}{S_o} \quad (3)$$

where τ_{atm} is the daytime atmospheric transmissivity for SW radiation (dimensionless) and S_o is the extraterrestrial solar radiation calculated following procedures recommended by ASCE (2005).

In the absence of clouds (clear sky), S_g approaches the theoretical maximum S_{go} which was estimated by Eq. (4) (ASCE, 2005).

$$S_{go} = \tau_o S_o = \left(0.75 + 2 \times 10^{-5} A\right) S_o \quad (4)$$

where S_{go} is the incident SW radiation under clear sky conditions, τ_o is the estimated atmospheric transmissivity under a clear sky (= 0.754) and A is the local altitude (218 m asl). The S_{go} calculation was used during quality control and assessment of measured S_g following recommendations of ASCE (2005).

Due to the high predominance of days with clouds in both years, the following criterion involving τ_{atm} was used to distinguish the degree of daytime cloudiness over the experimental area: $\tau_{atm} < 0.20$ (completely cloudy or overcast sky - CCS), $0.20 \leq \tau_{atm} < 0.45$ (mostly cloudy sky - MCS), $0.45 \leq \tau_{atm} < 0.70$ (mostly sunny sky - MSS) and $\tau_{atm} \geq 0.70$ (completely sunny or clear sky - CSS). Despite being an arbitrary classification, the use of τ_{atm} allowed us to define quantitative boundaries among the classes of cloud fractions rather than collecting visual observations of sky cover.

3. Results and Discussion

3.1. Atmospheric conditions and water turbidity

Data collected by instruments in the WT from 7th Aug. to 29th Dec. 2015 (145 days) and from 10th Sept. to 31st Dec. 2016 (113 days) were selected to characterize the local atmospheric conditions (Table 1). These time period represent late winter to early summer.

The atmospheric transmissivity (τ_{atm}) calculated from daily mean values of S_g and S_o (Eq. (3)) ranged from 0.185 to 0.733 in 2015 and from 0.219 to 0.679 in 2016. In 2015, there was one day with CCS conditions (≈ 0.7% of the period), 18 days with MCS (12%), 113 days with MSS (68%), and 13 days with CSS (9%). These percentages in 2016 were 0 (no day), 26% (29 days), 74% (84 days), and

Table 1 - Summary of daily weather conditions at the experimental site in the 2015 and 2016 campaigns based on measurements made at the weather tower.

Year	Air temperature (°C)			Relative humidity (%)		Rain depth (mm)	Wind speed (m/s)[a]	Incoming solar radiation (MJ/m^{2}day)		
	Max.[b]	Min.[b]	Mean	Max.	Min.	Total	Mean	Max.	Min.	Mean
2015	38.1	15.9	24.5	98	32	101	2.7	29.4	7.3	21.7
2016	34.0	19.7	24.9	100	35	146	2.6	27.1	8.3	20.0

[a]Wind measured at 7 m above ground in 2015 and 3 m above ground in 2016.
[b]Temperature of the hottest and coldest days.

0 (no day), respectively. The predominance of days with cloud cover in the region is due to its proximity to the Atlantic Ocean coast (about 60 km in the southeast direction), which produces persistent cloudiness conditions most of the time.

Due to technical problems, the turbidimeter did not work as expected in 2015 but in 2016 water turbidity measurements were made continuously for 74 days (18th Sept. to 30th Nov.). Hourly values of turbidity ranged from 1.7 to 5.4 NTU (average of 2.6 NTU), showing an increasing linear trend over time. As mentioned, the low turbidity water (high transparency) in the farm irrigation reservoirs comes from filtration of organic and mineral fine particles followed by reverse osmosis. Therefore, penetration of the blue-green portion of shortwave radiation is expected to be relatively deep (Jensen and Allen, 2016), and, in the case of the clear ponds with black plastic membranes, most of that portion of SW would be absorbed by the black liner.

3.2. Seasonal analysis of radiation balance components

The period of measurements in the raft in 2015 covered 175 days (from 11th Jun. to 2nd Dec.) but in 2016 this interval was shorter (74 days, from 18th Sept. to 30th Nov.) due to technical problems that delayed sensor deployment. Unlike 2016, failures in data collection occurred in 2015, especially in the first half of the period. Thus, the 74-day period of 2016 in common with 2015 was used for comparison purposes. Table 2 summarizes daily mean values for all components of the radiation balance. To facilitate comparisons, all fluxes shown are positive. It is common, however, to consider radiative fluxes oriented toward the surface as positive and as negative those in the opposite direction (Shuttleworth, 2012). In general, the values were quite similar between both years. Reflection of SW radiation (10.3 W/m^2 on average) was very small compared to the incident flux (245.8 W/m^2), indicating that the low-turbidity water in the farm has a high capacity for absorbing solar radiation.

Figure 2, showing data from the 2016 campaign only, illustrates the time variation of the radiation balance components. Incoming fluxes were plotted as positive and outgoing ones as negative. To better visualize variations in the S_r and L_r curves, the values were multiplied by a factor of 10.

For the entire period, absolute L_e was greater in magnitude than L_{atm} and, therefore, L_{net} (Fig. 2B) was consistently negative with a 53.5 W/m^2 daily average (Table 2). This indicates that the surface lost more long-

Table 2 - Mean and amplitude (range) values of 24-h radiation balance components at the low-turbidity water surface in 2015 and 2016 campaigns from 18th Sept. to 30th Nov.

Year	Statistics	Radiation flux density (W/m^2)							
		S_g	S_r	S_{net}	L_{atm}	L_r	L_e	L_{net}	R_n
2015	Mean (Range)	249.9 (83-321)	11.5 (5-14)	238.4 (78-308)	398.8 (374-429)	11.9 (11-13)	443.3 (431-458)	56.7 (33-76)	181.7 (41-244)
2016	Mean (Range)	241.7 (101-328)	9.1 (5-11)	232.6 (95-317)	402.4 (368-433)	12.0 (11-13)	443.8 (434-451)	53.5 (26-81)	179.2 (64-252)
Both	Mean	245.8	10.3	235.5	400.6	11.9	443.5	55.1	180.4

S_g = incoming SW radiation; S_r = reflected SW radiation; S_{net} = net SW radiation; L_{atm} = incoming LW radiation; L_r = reflected LW radiation; L_e = emitted LW radiation; L_{net} = net LW radiation, and R_n = net all-wave radiation.

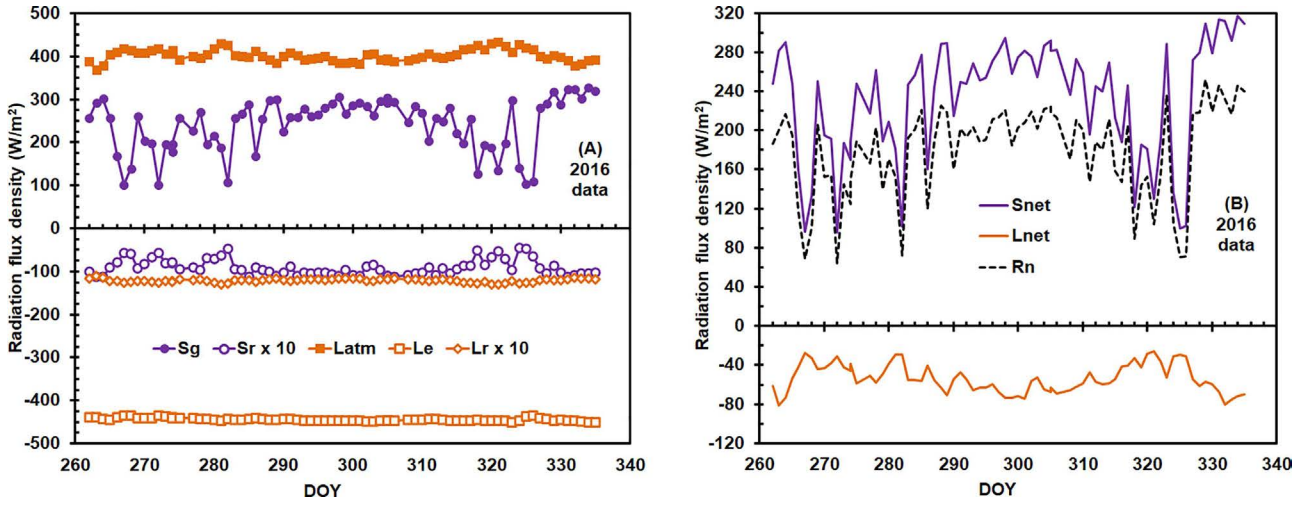

Figure 2 - Seasonal variation of daily components of the radiation balance over the surface of the low-turbidity water from 18th Sept. (DOY 262) to 30th Nov. 2016 (DOY 335).

wave radiation than it gained from the atmosphere in that period. Figure 2A shows that the L_{atm} data series had greater variability (13.7 W/m^2 std. dev.) than did L_e (3.7 W/m^2 std. dev.), reflecting impacts of changes in cloud cover that govern atmospheric emission as well as effects of air temperature oscillations relative to water temperature. In 2016, the mean temperature of water surface (T_w = 27.3 °C) was higher than that of air (T_a = 24.9 °C) and varied from 26.0 °C to 28.2 °C while for the air it varied from 21.8 °C to 27.2 °C.

Cloudiness caused variability in S_g and S_{net} as well as in R_n (Fig. 2). As previously mentioned, there were no completely clear sky days over the area in 2016. While S_{net} was always positive over time, L_{net} was always negative, which typically occurs over natural surfaces. The daily net all-wave radiation R_n was always positive ($S_{net} > L_{net}$), with negative values observed during nighttime and positive ones during daytime. The S_{net} and R_n curves followed the S_g variation closely and, on average, R_n corresponded to 74% of S_g (77% of S_{net}), evidencing the smaller contribution of the net LW balance (L_{net}) to R_n.

3.3. Detailed effects of cloud cover

Two days from each year with contrasting daytime atmospheric transmissivity (τ_{atm}) were selected to explore the effects of cloud cover on the radiation balance for the low-turbidity water surface. Table 3 summarizes, in decreasing order of τ_{atm}, the statistics for the selected days, namely, 4th Sept. 2015 (DOY 247), 5th Nov. 2016 (DOY 310), 12th Oct. 2016 (DOY 286), and 30th Oct. 2015 (DOY 303). For these days, τ_{atm} was 0.72, 0.55, 0.36, and 0.18, respectively.

As expected, SW radiation components were strongly affected by the presence of clouds. From CSS (completely sunny sky, τ_{atm} = 0.72) to CCS conditions (completely cloudy sky, τ_{atm} = 0.18), S_g varied from 278.1 W/m^2 to 83.4 W/m^2, a 70% reduction. Similar percent reductions in S_r and S_{net} were also observed, as shown in Table 3.

The atmospheric emission of LW radiation (L_{atm}) showed an increasing trend with cloud cover from 364.1 W/m^2 to 415.2 W/m^2, a 14% variation. The presence of clouds increases atmospheric emissivity (ε_{atm}) due to generally lower altitudes of clouds compared to the net altitude of emitting clear air columns (Carmona *et al.*, 2014; Aimi et *al.*, 2021). LW emission is also higher from clouds due to their generally higher temperature compared to an emitting clear air column. This is governed by the emission of LW radiation being proportional to its emissivity and the fourth power of its absolute temperature according to Stefan-Boltzmann's law (Moene and Van Dam, 2014).

The LW radiation emitted by the low-turbidity water surface (L_e) showed no trend and differences among the four days were small (11 W/m^2 range) due to probably similar T_w values observed in all days. Both L_e and L_{net} were influenced by T_w, which in turn depends, among many factors, on the aerodynamic conditions at the surface-atmosphere interface, as wind speed generates turbulence and mixing. The LW radiation reflected by water, L_r, followed the same trend as for L_{atm}, since the earlier was set as a constant fraction of the latter (Eq. (2)). The behavior of outgoing LW radiation (L_r + L_e) showed no trend with cloud cover relative to the behavior of L_{atm}. This resulted in L_{net} also decreasing with the degree of cloudiness, a reduction of about 54%.

Since S_g is the main input for the net all-wave radiation R_n, higher values of R_n at water surface were observed under higher τ_{atm} indicating impacts of higher availability of shortwave energy under clear or near clear sky conditions. A large fraction of this energy is transmitted and absorbed within the water body before eventually reaching the bottom of the reservoir. On the other hand, R_n increased from DOY 247 (τ_{atm} = 0.72) to DOY 310 (τ_{atm} = 0.55) because while reduction in S_g was only 9.2 W/m^2, the increase in the LW input (L_{atm}) was almost four times more (33.7 W/m^2) due to the effects of relatively warm clouds. As can be seen from Table 3, on a daily basis, LW fluxes were higher than SW fluxes, espe-

Table 3 - Mean absolute values of the radiation balance components measured over a low-turbidity water surface during the 2015 and 2016 campaigns using four selected example days with contrasting daytime cloud cover.

Radiation flux density (W/m^2)	CSS (τ_{atm} = 0.72) DOY 247/2015	MSS (τ_{atm} = 0.55) DOY 310/2016	MCS (τ_{atm} = 0.36) DOY 286/2016	CCS (τ_{atm} = 0.18) DOY 303/2015
S_g	278.1	268.9	169.1	83.4
S_r	12.6	10.2	9.1	5.1
S_{net}	265.6	258.7	160.1	78.3
L_{atm}	364.1	397.8	411.7	415.2
L_r	10.9	11.9	12.3	12.5
L_e	434.4	444.4	439.9	440.3
L_{net}	81.2	58.5	40.5	37.5
R_n	184.3	200.2	119.6	40.8

CSS = completely sunny (clear) sky; MSS = mostly sunny sky; MCS = mostly cloudy sky; CCS = completely cloudy (overcast) sky.

cially under cloudy conditions, indicating the importance of measurement or estimation of LW radiation in R_n calculations. However, the net contribution of SW components to R_n is more relevant since opposite fluxes of LW radiation (downward L_{atm} and upward L_e) tend to offset each other (Jensen and Allen, 2016) as also reported by Gianniou and Antonopoulos (2007) over Lake Vegoritis in Greece.

Figure 3 illustrates the time distribution of the radiation balance components for the four days in Table 3, including the envelope of clear-sky solar radiation S_{go} for reference (Eq. (4)). As in Fig. 2, values for S_r and L_r were multiplied by 10 for the sake of clarity. As expected, the reduction in S_g compared to S_{go} increased as the cloud cover increased. On DOY 247 the reduction was just 7% (from S_{go} = 299.3 W/m^2 to S_g = 278.1 W/m^2) followed by 22% on DOY 310, 50% on DOY 286, and finally 76% reduction on DOY 303 when the sky was covered by dense clouds all day. On this last day, S_g (average 83.4 W/m^2) was much smaller than the maximum expected S_{go} (average 343.2 W/m^2). In all days, R_n followed S_g very closely, regardless of the degree of cloud cover, with R_n experiencing a reduction of about 78% from the clear sky to the overcast sky (Table 3). On the day with the highest atmospheric transmissivity (DOY 247, τ_{atm} = 0.72), S_g peaked above S_{go} envelope at around 1100 h probably due to nearby clouds that reflected additional shortwave radiation upon the pyranometer (Allen, 1996).

Figure 3 also shows that the degree of cloudiness affected not only the amount of solar radiation reflected by the water surface (a daily average reduction of 59% from clear to overcast sky as shown in Table 3) but the shape of the S_r curve. On DOY 247 (clear sky), the maximum values for S_r were concentrated on times of the day having low sun angle (early in the morning and late afternoon) while it was relatively constant in between. The opposite was observed on DOY 303 (overcast sky), when S_r peaked around noon with the minimum values at times of low sun angles. Under such conditions, S_r was less early in the

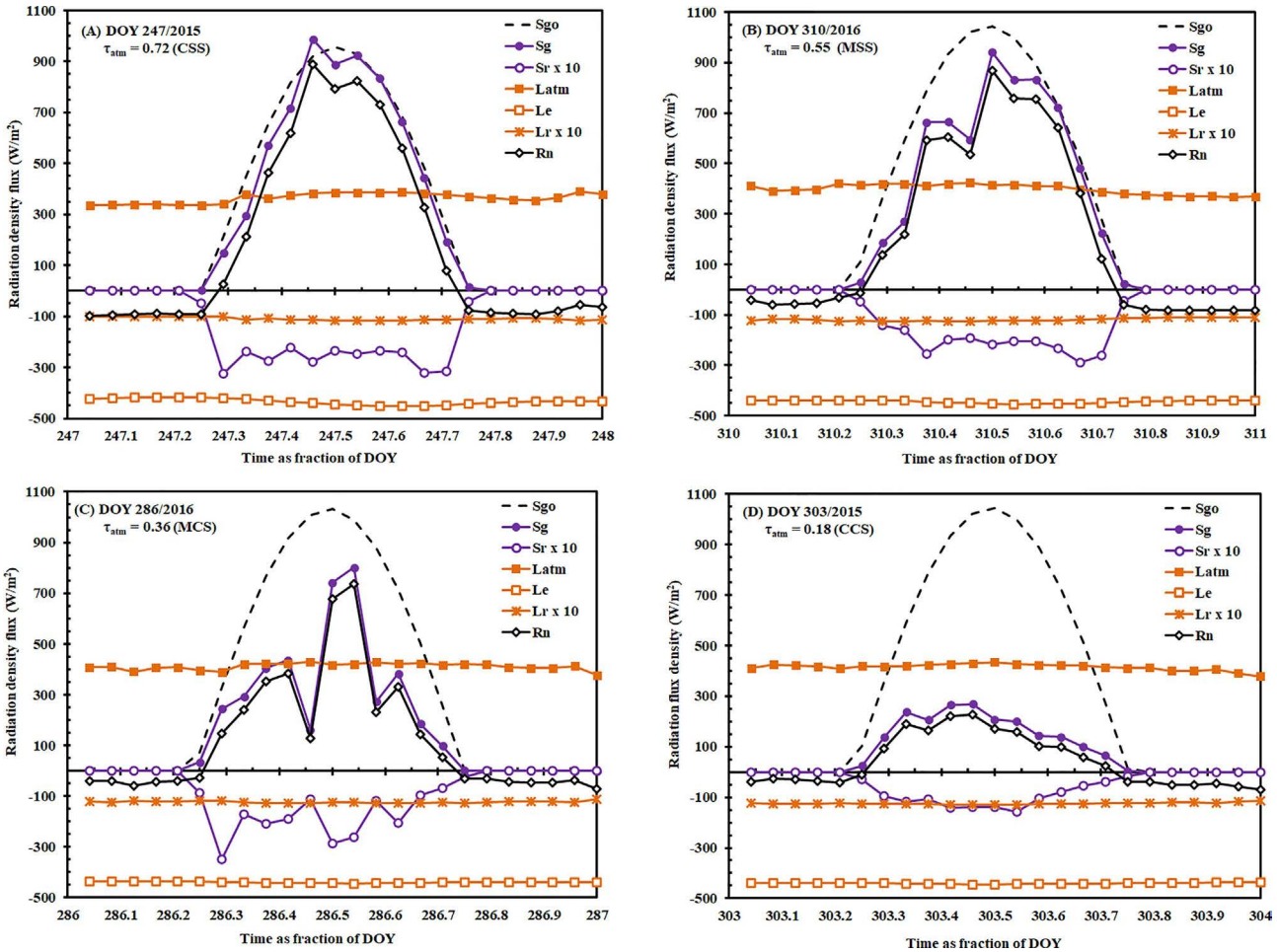

Figure 3 - Daily course of radiation balance components on the surface of low turbidity water as a function of cloud cover expressed by τ_{atm} (the daytime atmospheric transmissivity) for the four selected days from 2015 and 2016. CSS = completely sunny (clear) sky, MSS = mostly sunny sky, MCS = mostly cloudy sky, and CCS = completely cloudy (overcast) sky.

morning and late afternoon compared to DOY 247 since clouds blocked solar radiation reducing S_g. The S_r peaked around noon on DOY 303 because under high cloudiness it is expected that diffuse radiation coming from all angles of the hemispherical sky reaches the surface in higher proportion compared to the direct beam (Katsaros *et al.*, 1985).

Within a day, the LW emission by atmosphere and water surface did not experience significant variations over the course of 24 hours. However, comparing the two extreme cases for daytime atmospheric transmissivity (Figs. 3A and 3D), daily amplitude for L_e was more pronounced compared to L_{atm}. On DOY 247 (τ_{atm} = 0.72), the 54 W/m^2 range for L_{atm} (min = 336 W/m^2 and max = 390 W/m^2) was slightly lower compared to DOY 303 (τ_{atm} = 0.18) with a range of 57 W/m^2 (min = 378 W/m^2 and max = 435 W/m^2) but L_e ranged much more (36 W/m^2, max = 454 W/m^2 and min = 418 W/m^2) on DOY 247 relative to DOY 303 (8 W/m^2, max = 444 W/m^2 and min = 436 W/m^2). Larger ranges for L_e observed on a clear day compared to a cloudy day is because during daytime on a clear day, the upper water layer is heated more intensively by solar radiation which increases its temperature and radiation emission. During nighttime it loses more radiation as LW emission, therefore decreasing its temperature.

The daily amplitude in R_n decreased with cloud cover, the same trend for the SW components of the radiation balance. On DOY 247, R_n varied from 889 W/m^2 to -98 W/m^2 and from 228 W/m^2 to -70 W/m^2 on DOY 303. The average nighttime values for R_n were -46 W/m^2, -34 W/m^2, -23 W/m^2, and -22 W/m^2 on DOYs 247, 310, 286, and 303, respectively.

Figure 4 summarizes an analysis of seasonal and daily courses for water and air temperatures (respectively, T_w and T_a) with data from 2015. Figure 4A shows how hourly data for T_w and T_a varied within each day from the 21st July (DOY 202) to 2nd Dec. (DOY 336), encompassing most parts of winter and spring in the southern hemisphere. T_w was measured with the infrared thermometer depicted in Fig. 1A and T_a was measured at 2 m height in the WT deployed in between adjacent irrigation tanks. It can be seen from Fig. 4A that T_a was consistently below T_w except around noon when T_a peaked above T_w for most days, mainly from mid-October. For a few days, T_a peaked quite below T_w probably due to colder air masses entering the region which is common in the winter time.

Some of the elevation of T_a over T_w was caused by heating of surface air by land surfaces upwind of the ponds during afternoon and by evaporative cooling of the pond surfaces. Early morning and late afternoon when solar radiation is less, T_a was typically well below T_w. Additionally, for all days during the period, the daily amplitude in T_a (ΔT_a) was substantially higher than that for T_w (ΔT_w). The resistance of water in changing temperature in the irrigation tank is due to its depth and its higher heat capacity compared to air (water 4180 kJ/(m^{3}K) and air 1.2 kJ/(m^{3}K) at 25 °C).

According to Fig. 4A, on average, both T_w and T_a tended to increase over time as the days passed from winter to spring, reflecting the availability of energy at the surface. Based on daily mean values, in 132 out of 135 days, T_w was higher than T_a. The difference between daily T_w and T_a varied from -0.2 °C to 8.6 °C, with an average of 4.4 °C. For the entire 2015 season (Fig. 4A), daily mean T_w was 26.1 °C (max = 29.0 °C, min = 23.3 °C) compared to daily mean T_a on the order of 21.8 °C (max = 26.3 °C, min = 18.7 °C). These outcomes illustrate the strong influence of warming of the water surface by near-surface absorption of infrared and near-infrared radiation (Jensen and Allen, 2016) relative to the overlying air.

The impact of cloud cover on daily variation of T_w and T_a is shown in more detail in Fig. 4B for the four selected days from Table 3. As already shown in Fig. 4A, in general, T_w was higher than T_a most of the time regardless the cloud cover, especially during nighttime. Daily mean temperatures for water and air did not follow any

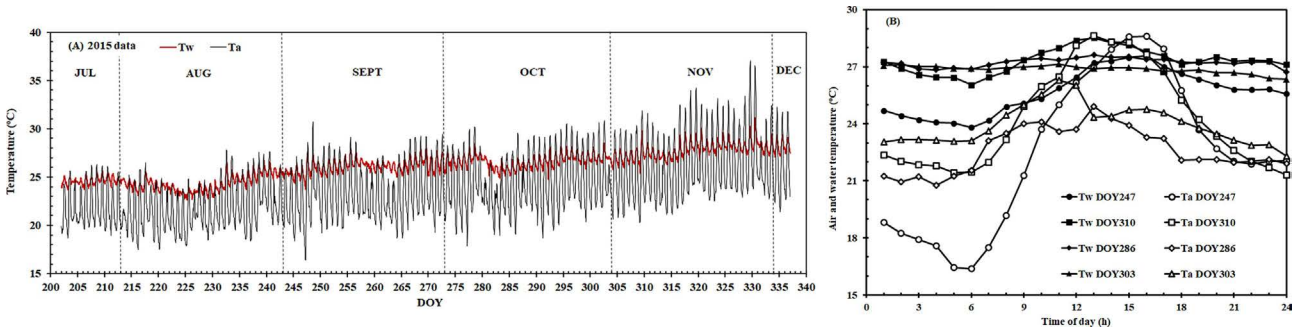

Figure 4 - Time trends in water surface (T_w) and air (T_a) temperatures from mid-July to early December 2015 and T_w and T_a course for the selected days with contrasting cloud cover. DOY 247/2015 (CSS, τ_{atm} = 0.72), DOY 310/2016 (MSS, τ_{atm} = 0.55), DOY 286/2016 (MCS, τ_{atm} = 0.36), and DOY 303/2015 (CCS, τ_{atm} = 0.18). CSS = completely sunny (clear) sky, MSS = mostly sunny sky, MCS = mostly cloudy sky, and CCS = completely cloudy (overcast) sky.

noticeable trend with cloud cover, which suggests that average temperature near or at the water surface area affected by other factors besides cloudiness. However, this is not the case for daily range in temperature (ΔT) as can be deduced from Fig. 4B, because for both water and air, ΔT decreased as cloud cover increased. ΔT_w varied from 3.8 °C (DOY 247, τ_{atm} = 0.72) to 0.8 °C (DOY 303, τ_{atm} = 0.18) and ΔT_a varied from 12.3 °C (DOY 247) to 4.0 °C (DOY 303). In fact, T_w virtually did not change over time on DOYs 286 and 303, the two days having the highest cloud cover. This was due to the reduction in shortwave energy during daytime and consequent warming of water, as well as moderation of effective sky temperature by clouds. This atmospheric condition affected T_a as well, since those days had the lowest ΔT_a. The presence of clouds seems to make the pattern in temperature variation over time unclear for both T_w and T_a, which means that the moments of occurrence of daily maximum and minimum temperatures cannot be precisely predicted as for clear or nearly clear sky days.

4. Final Considerations

In this study, data on water turbidity, radiation balance, and skin temperature were analyzed from measurements made in 2015 and 2016 in the center of a farm pond that stored low-turbidity water for irrigation of a special variety of tobacco in eastern Bahia, Brazil. Valid water turbidity readings were obtained only during the 2016 season and remained at very low (2.6 NTU on average).

The absorption of shortwave (SW) radiation by water was high and corresponded to about 96% of incident SW radiation (S_g). During both seasons, daily longwave (LW) emission upward from the water surface (L_e) remained higher than that for downward LW radiation (L_{atm}), making the net LW radiation (L_{net}) consistently negative (-55.1 W/m^2 on average). The net all-wave radiation (R_n) corresponded to 77% of net SW radiation (S_{net}), evidencing a smaller contribution from L_{net} to R_n.

Analysis on four selected days of contrasting τ_{atm} (0.72 - clear sky, 0.55, 0.36, and 0.18 - overcast sky) showed that the degree of cloudiness decreased S_g by 70% while the effect on L_{atm} was the opposite, increasing by 14%. The S_{net} and S_r components in the radiation balance decreased with cloud cover, following the same trend in S_g, resulting in 70.5% and 59% reductions, respectively. R_n followed S_g very closely regardless the degree of cloud cover with R_n experiencing a reduction of about 78% from the clear to the overcast sky. Within the course of a day, the L_e and L_{atm} components experienced slight variation over 24 h, but, in general, for all four days, both atmospheric and water LW emission varied little as cloud cover increased.

The measurement of air and water surface temperature (T_a and T_w, respectively) in 2015 (having a longer measurement season with 135 days) revealed that T_a was consistently below T_w except during afternoon, with T_a showing a daily amplitude higher compared to T_w. During the 2015 season, daily mean T_w was 26.1 °C (max = 29.0 °C, min = 23.3 °C) and daily mean T_a on the order of 21.8 °C (max = 26.3 °C, min = 18.7 °C). In general, not only did the air show higher temperature variation over 24 h as compared to the low-turbidity water, but T_w was higher than T_a most of the time, especially at nighttime.

Acknowledgment

The authors manifest their appreciation to the *Fundação de Amparo à Pesquisa do Estado da Bahia / State of Bahia Foundation for Scientific Research* (FAPESB) for the financial support through a research grant (TO APP0075/2011) and doctorate scholarship (TO BOL0545/2013) to the first author without which this research would not have been possible. Support from the Idaho Agricultural Experiment Station (IDA01620) and Nebraska Agricultural Experiment Station is acknowledged.

References

AIMI, D.; ZIMMER, T.; BULIGON, L.; SOUZA, V. de A.; HERNANDEZ, R.; ROMIO, L.; *et al.* Evaluation of atmospheric downward longwave radiation in the Brazilian Pampa Region. **Atmosphere**, v. 12, n. 1, p. 1-17, 2021. doi

ALLEN, R.G. Assessing integrity of weather data for reference evapotranspiration estimation. **Journal of Irrigation and Drainage Engineering**, v. 122, n. 2, p. 97-106, 1996. doi

ALVARES, C.A.; STAPE, J.L.; SENTELHAS, P.C.; GONÇALVES, J.L. de M.; SPAROVEK, G. Koppen's climate classification map for Brazil. **Meteorologische Zeitschrift**, v. 22, n. 6, p. 711-728, 2013. doi

AYDIN, H.; KARAKUS, H. Estimation of evaporation for Lake Van. **Environmental Earth Sciences**, v. 75, 1275, 2016. doi

ASCE. **The ASCE Standardized Reference Evapotranspiration Equation**. Reston: ASCE, 205 p., 2005.

BLONQUIST JR, J.M.; TANNER, B.D.; BUGBEE, B.D. Evaluation of measurement accuracy and comparison of two new and three traditional net radiometers. **Agricultural and Forest Meteorology**, v. 149, n. 10, p. 1709-1721, 2009. doi

BORGES, T.K.S. **Evaporação em Superfície de Água Livre Com Baixa Turbidez**. Tese de Doutorado em Engenharia Agrícola, Universidade Federal do Recôncavo da Bahia, Cruz das Almas, 120 p., 2017.

BORGES, T.K.S.; OLIVEIRA, A.S. de; SILVA, N.D. da; SANTANA, C.E. Plataforma flutuante de baixo custo para pesquisas em micrometeorologia e qualidade da água em reservatórios. **Revista Geama**, v. 4, n. 1, p. 38-45, 2016.

CAMPBELL SCIENTIFIC. **CNR4 Net Radiometer Instruction Manual**. 2014. Disponível em https://s.campbellsci.com, acesso em 23 out. 2015.

CARMONA, F.; RIVAS, R.; CASELLES, V. Estimation of daytime downward longwave radiation under clear and cloudy skies conditions over a sub-humid region. **Theoretical and Applied Climatology**, v. 115, n. 1-2, p. 281-295, 2014. doi

DAVIES, J.A.; ROBISON, P.J.; NUNEZ, M. Field determinations of surface emissivity and temperature for Lake Ontario. **Journal of Applied Meteorology**, v. 10, n. 4, p. 811-819, 1971. doi

DAVIES-COLLEY, R.J.; SMITH, D.G.Turbidity, suspended sediment, and water clarity: A review. **Journal of American Water Resources Association**, v. 37, n. 5, p. 1085-1101, 2001. doi

FINCH, J.W.; HALL, R.L. Evaporation from lakes. In: ANDERSON, M.G.; McDONNEL, J.J. (orgs.). **Encyclopedia of Hydrological Sciences**. Chichester: Wiley, p. 635-646, 2005.

GALLEGO-ELVIRA, B.; BAILLE, A.; MARTÍN-GÓRRIZ, B.; MARTÍNEZ-ÁLVAREZ, V. Energy balance and evaporation loss of an agricultural reservoir in a semi-arid climate (south-eastern Spain). **Hydrological Processes**, v. 24, p. 758-766, 2010. doi

GIANNIOU, S.K.; ANTONOPOULOS, V.Z. Evaporation and energy budget in Lake Vegoritis, Greece. **Journal of Hydrology**, v. 345, n. 3-4, p. 212-223, 2007. doi

JENSEN, M.E.; ALLEN, R.G. **Evaporation, Evapotranspiration, and Irrigation Water Requirements**. Reston: ASCE, 769 p., 2016.

KATSAROS, K.B.; McMURDIE, L.A.; LIND, R.L.; DEVAULT, J.E. Albedo of a water surface, spectral variation, effects of atmospheric transmittance, sun angle and wind speed. **Journal of Geophysical Research**, v. 90, n. C4, p. 7313-7321, 1985. doi

KIPP & ZONEN. **CNR4 Net Radiometer Instruction Manual, V. 1409**, 2010. Disponível em http://kippzonen.com, acesso em 23 set. 2015.

KOHSIEK, W.; LIEBETHAL, C.; FOKEN, T.; VOGT, R.; ONCLEY, S.P.; *et al.* The energy balance experiment EBEX-2000. Part III: Behaviour and quality of the radiation measurements. **Boundary-Layer Meteorology**, v. 123, p. 55-75, 2007. doi

LIU, H.; FENG, J.; SUN, J.; WANG, L.; XU, A. An eddy covariance measurements of water vapor and CO_2 fluxes above the Erhai Lake. **Science China Earth Sciences**, v. 58, n. 3, p. 317-328, 2015. doi

MARQUIS, P. Turbidity and suspended sediment as measures of water quality. **Streamline Watershed Management Bulletin**, v. 9, n. 1, p. 21-23, 2005.

MOENE, A.F.; VAN DAM, J.C. **Transport in the Atmosphere-Vegetation-Soil Continuum**. New York: Cambridge University Press, 433 p., 2014.

MONTEITH, J.L.; UNSWORTH, M.H. **Principles of Environmental Physics**. New York: Academic Press, 418 p., 2013.

OKE, T.R. **Boundary Layer Climates**. London: Routledge, 464 p., 1995.

SILVA, J.B.; GAIO, D.C.; CURADO, L.F.A.; NOGUEIRA, J. de S.; VALLE JÚNIOR, L.C.G.; *et al.* Evaluation of methods for estimating atmospheric emissivity in Mato-Grossense Cerrado. **Revista Ambiente & Água**, v. 14, n. 3, p. 1-12, 2019. doi

SHUTTLEWORTH, W.J. **Terrestrial Hydrometeorology**. Chichester: Wiley-Blackwell, 448 p., 2012.